Available online at www.sciencedirect.com

ScienceDirect

Advances in Space Research 66 (2020) 974–991

ADVANCES IN SPACE RESEARCH (a COSPAR publication)

www.elsevier.com/locate/asr

Hybrid removal of end-of-life geosynchronous satellites using solar radiation pressure and impulsive thrusts ☆

Hao Mei [a,*], Christopher J. Damaren [a], Xingqun Zhan [b]

[a] University of Toronto Institute for Aerospace Studies, 4925 Dufferin Street, Toronto, Ontario M3H 5T6, Canada
[b] Shanghai Jiaotong University School of Aeronautics and Astronautics, 800 Dongchuan Road, Shanghai 200240, China

Received 11 November 2019; received in revised form 3 April 2020; accepted 30 April 2020
Available online 12 May 2020

Abstract

This paper proposes an analytical solution of removing end-of-life GEO satellites to the GEO graveyard region using solar radiation pressure (SRP) and impulsive thrusts. The dynamic model of a GEO satellite equipped with a solar sail is first built upon the magnitude comparisons of different accelerations exerted on the satellite. Then the dynamic system is constructed based on the Gauss's Variation of Parameter (VOP) equations, and linearized along a nominal trajectory. Control angles of the sail and impulsive thrust vectors are generated using the proposed optimal hybrid disturbance-accommodation tracking maneuvers. Simulations indicate that, to remove a satellite in 360 days using only SRP with the proposed method, a minimal area-to-mass (A/M) ratio of 0.13 m^2/kg is required. When the A/M ratio of spacecraft is smaller than the minimal value, impulsive thrusts are applied to assist the removal process. For a satellite with an A/M ratio of 0.1 m^2/kg, a total impulse of 10.5 m/s is required.

Keywords: GEO debris removal; Optimal hybrid control; Disturbance accommodation tracking; Solar radiation pressure; Impulsive thrusts

1. Introduction

Geostationary Earth Orbit (GEO), an equatorial circular orbit with a radius of about 42164.5 km, is a precious and limited orbit resource. Satellites in GEO remain stationary to the rotating Earth, which makes GEO very favorable for communication, navigation, and Earth-observation missions. However, during the last 50 years of use, GEO has become more and more crowded. The "Galaxy 15 incident" (Allen, 2010) implies that, without further orbit control, nonfunctional satellites may drift because of luni-solar disturbances, allowing them to wander the GEO belt and threaten active satellites (Rosengren et al., 2015).

The increasing population of GEO debris has been alarming in recent years (Anselmo and Pardini, 2008; Johnson, 2012; Anderson and Schaub, 2014). The latest annual report "Classification of Geosynchronous Objects" (ESA, 2018) published by European Space Agency (ESA) indicates that the number of all the known space debris in the geosynchronous region has been increasing since 2001, and exceeded 1000 in 2018. Debris takes up about 70% of the total object amount, and about 3/4 of them reside in drift orbits. The report also shows that the debris in drift orbits are oscillating around GEO, causing enormous risk for operational satellites. Collision probability analysis in geosynchronous orbits (McKnight and Di Pentino, 2013; Frey et al., 2017; Oltrogge et al., 2018) shows that the collision probability between debris and operational satellites cannot be underestimated. The latest

☆ Funding: This work was supported by the China Scholarship Council (CSC)
* Corresponding author.
E-mail addresses: hao.mei@mail.utoronto.ca (H. Mei), damaren@utias.utoronto.ca (C.J. Damaren), xqzhan@sjtu.edu.cn (X. Zhan).

https://doi.org/10.1016/j.asr.2020.04.052
0273-1177/

collision likelihood assessment (Oltrogge et al., 2018) indicates that the collision probability in the GEO ring is as much as four orders of magnitude higher than previously believed. A collision is likely to occur every 4 years for one satellite out of the entire GEO active satellites against a 1 cm Resident Space Object (RSO), and every 50 years against a 20 cm RSO. Furthermore, the relative collision velocities can be as high as 4 km/s.

To encounter the severe situation, the Inter-Agency Space Debris Coordination Committee (IADC) published Space Debris Mitigation Guidelines (IADC, 2007) in 2007, aimed at limiting the generation of space debris in the environment. According to the guidelines, the GEO protected region (Table 1) should be protected in respect of space debris generation. End-of-life satellites in GEO should be maneuvered far enough above GEO so as not to interfere with the GEO protected region. Studies (Chao, 1998; Gopinath and Ganeshan, 2005) have found that fulfilling the two conditions in Table 2 (which also define the GEO graveyard region) at the end of disposal will ensure an orbit that remains above the GEO protected region. Only about 40% of end-of-life GEO satellites have been successfully re-orbited to the GEO graveyard orbits (ESA, 2018).

The current GEO debris mitigation technique can be classified into four categories, namely, removing debris using thrusts, SRP, ion-beam irradiation, and laser system.

ESA has issued the Robotic Geostationary Orbit Restorer (ROGER) (Kassebom, 2003; ESA, 2003) system in 2003. The re-orbit mission is achieved by first capturing inactive satellites with a net or tethered gripper, then pulling them into the graveyard orbits. The ROGER system has a launch mass of 3,500 kg and a propellant mass of about 2700 kg. It is designed to re-orbit up to 30 debris, with 2–3 months for each one. To avoid hard-contact between re-orbiter and debris when debris is non-cooperative (i.e. large or rotating), Schaub proposed the Geosynchronous Large Debris Re-orbiter (GLiDeR) (Schaub and Moorer, 2012) in 2012. GLiDeR uses active charge emission to raise its own absolute potential to 10s of kilovolts and, in addition, directs a stream of charged particles at the debris to increase its absolute potential. In a puller configuration the opposite polarity of the debris creates an attractive force between the GLiDeR and the debris. Preliminary analysis shows that a 1000 kg debris object can be re-orbited over 2–4 months.

Borja first demonstrated the feasibility of using SRP as a propulsion source to re-orbit three-axis stabilized GEO satellites to the GEO graveyard region in 2006 (Borja and Tun, 2006). Kelly proposed the TugSat (Kelly et al., 2018) concept in 2018. A 50 kg CubeSat equipped with an 800 m^2 solar sail is used to re-orbit a 1000 kg nonfunctional satellite. Re-orbiting is accomplished by first increasing the apogee and raising the semi-major axis 350 km above the GEO altitude, then reducing the eccentricity of the orbit to zero and releasing the payload. Simulation shows that it takes about one year for TugSat to re-orbit a 1000 kg satellite.

Ion-beam irradiation has been proven as an effective way of space debris removal (Bombardelli and Pelaez, 2011; Merino et al., 2013). Kitamura proposed an ion-beam re-orbiter in 2014 (Kitamura et al., 2014). The re-orbiter, equipped with two ion engines, first approaches a debris object, then an ion-beam exhausted from one of the ion engines irradiates and directly pushes the debris to graveyard orbits. The other engine on the opposite side is operated so that the re-orbiter follows the debris during the re-orbiting process. Preliminary analysis shows that six debris objects can be re-orbited in 170 days. The re-orbiter has a launch mass of 2500 kg, and requires 7 kW of total power, 31 kg of Xenon propellant and 808 kN · s of total impulse.

In 2016, Phipps proposed a space-borne laser system to re-orbit GEO space debris to graveyard orbits (Phipps and Bonnal, 2016). The laser system, equipped with an electrical propulsion system, follows and remains 10 km west of the target debris during the whole re-orbit process. Two laser chasers are located on the same elliptical orbit, with perigee altitude 300 km above GEO, and apogee altitude 2047 km above GEO, and the two chasers are 180° from each other. The first station raises the apogee of the debris, then the second station tends to circularize it. Each station

Table 1
The GEO protected region.

Property	Requirement
GEO	35786 km
Upper bound	GEO + 200 km
Lower bound	GEO − 200 km
Inclination	[−15°, +15°]

Table 2
The GEO graveyard region.

Property	Requirement
Perigee altitude	A minimum increase of 235 km + $(100 \cdot C_R \cdot A/m)$
	235 km: the sum of the upper altitude of the GEO protected region (200 km) and the maximum descent due to luni-solar and geopotential perturbations (35 km) C_R : the solar radiation pressure (SRP) coefficient A/m : the area to dry mass ratio
Eccentricity	$[0, 0.003]$

requires a total power of 36 kW. Preliminary analysis shows that one derelict GEO satellite can be re-orbited in 75 days.

From the state-of-the-art of end-of-life GEO satellite removal one can see that removing GEO satellites using only thrusts uses a large amount of propellant (2700 kg in the ROGER system), while removing using only SRP requires a large area solar sail (800 m^2 in the TugSat). To avoid the difficulty of deploying and maneuvering a large area solar sail, and also considering the fact that there will be a small amount of propellant left when a GEO satellite fulfills its mission and reaches end-of-life (Pelton and Jakhu, 2010, Chap 10.4), this works is aimed at proposing a hybrid removal method which makes use of this small amount of propellant and also requires a relatively smaller area for the solar sail.

This work first proposes an analytical solution of removing end-of-life GEO satellites to the GEO graveyard region using SRP. When the A/M ratio of satellite is small, impulsive thrusts are applied to assist the removal process. The paper is organized as follows. Section 2 presents an accurate dynamic model of a GEO satellite equipped with a solar sail. The dynamic system is modelled and linearized in Section 3, and the linearization is used to derive the optimal hybrid disturbance-accommodation, desired-trajectory-tracking maneuver in Section 4. Simulations are presented and analyzed in Section 5, while Section 6 draws conclusions.

2. Spacecraft dynamics

The total acceleration exerted on a GEO satellite can be described as

$$\ddot{\boldsymbol{r}} = \ddot{\boldsymbol{r}}_{\oplus} + \ddot{\boldsymbol{r}}_{3} + \ddot{\boldsymbol{r}}_{\mathrm{SRP}} \tag{1}$$

where $\ddot{\boldsymbol{r}}_{\oplus}$ denotes the Earth gravitational acceleration, including the two-body acceleration and Earth gravitational perturbations, $\ddot{\boldsymbol{r}}_{3}$ is the third-body (the Sun and Moon) gravitational perturbation, and $\ddot{\boldsymbol{r}}_{\mathrm{SRP}}$ denotes the acceleration due to SRP.

Earth's gravitational potential is given by (Vallado, 2013, page 545)

$$\begin{aligned} U \quad &= \underbrace{\tfrac{u_{\oplus}}{r} - \frac{u_{\oplus}}{r}\sum_{l=2}^{\infty} J_l \left(\frac{R_{\oplus}}{r}\right)^{l} P_l[\sin\phi]}_{\text{zonal harmonics}} \\ &+ \underbrace{\frac{u_{\oplus}}{r}\sum_{l=2}^{\infty}\sum_{m=1}^{l}\left(\frac{R_{\oplus}}{r}\right)^{l} P_{l,m}[\sin\phi]\{C_{l,m}\cos(m\lambda_{sat}) + S_{l,m}\sin(m\lambda_{sat})\}}_{\text{sectoral and tesseral harmonics}} \end{aligned} \tag{2}$$

where $u_{\oplus}$ is the Earth's gravitational parameter, r the magnitude of the satellite position vector in the Earth Centred Earth Fixed (ECEF) frame, ϕ and λ are the latitude and longitude of satellite, P_l ($P_{l,m}$) denotes the conventional (associated) Legendre polynomials, and J_l ($C_{l,m}, S_{l,m}$) are the zonal (tesseral) harmonics. By taking the gradient of the total gravitational potential, Earth's gravitational acceleration in the ECEF frame can be calculated as

$$\ddot{\boldsymbol{r}}_{\oplus} = \vec{\nabla} U = \frac{\partial U}{\partial x}\vec{\boldsymbol{x}} + \frac{\partial U}{\partial y}\vec{\boldsymbol{y}} + \frac{\partial U}{\partial z}\vec{\boldsymbol{z}} \tag{3}$$

where $\vec{\boldsymbol{x}}, \vec{\boldsymbol{y}}, \vec{\boldsymbol{z}}$ denote the unit basis of the ECEF frame. Eq. (2) can be rewritten as

$$\begin{aligned} U = U_{two-body} &+ \underbrace{U_{J2} + U_{J3} + U_{J4}\cdots}_{\text{zonal terms}} \\ &+ \underbrace{U_{J22} + U_{J31} + U_{J32} + U_{J33} + U_{J41}\cdots}_{\text{sectoral and tesseral terms}} \end{aligned} \tag{4}$$

By varying the latitude of the spacecraft from $-90°$ to $90°$, and longitude from $0°$ to $360°$, the maximal magnitudes of perturbative accelerations due to different gravitational terms near GEO are calculated and presented in Fig. 1. It can be seen from Fig. 1 that the magnitudes of the second order terms of Earth's gravitational acceleration are comparable to that of SRP when A/M is around 0.1 km/s^2, while the magnitudes of the third order terms are close to that of SRP when A/M is equal to 0.001 km/s^2.

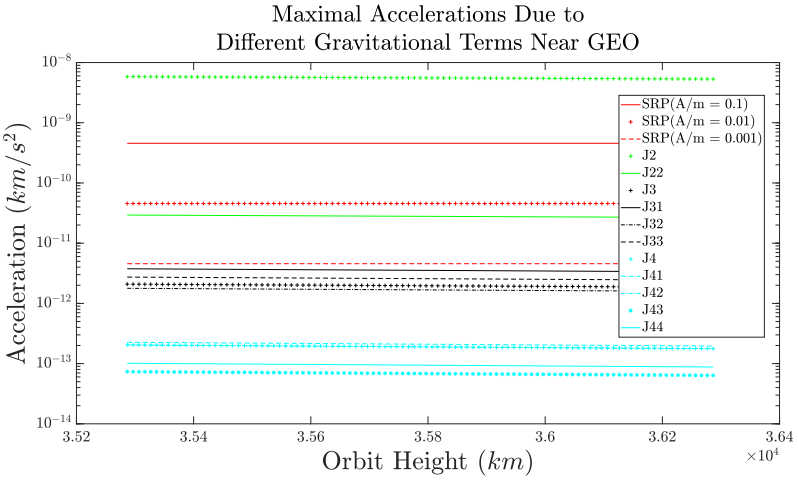

Fig. 1. Maximal accelerations due to different gravitational terms near GEO.

Since the removal time is around one year, even tiny perturbations may cause evident drift of orbital elements. To see this, the drift of the orbital elements in 360 days due to each gravitational term is simulated and presented in Fig. 2. From Fig. 2 we see that the J_{22} term and the J_{33} term cause relatively large semimajor axis drift, which reaches about 11 km and 6 km respectively. The eccentricity drift caused by the J_2 term is more evident than the others, which is still bounded by $3 \cdot 10^{-5}$. The inclination drifts are all small and bounded by $3 \cdot 10^{-6}$ degrees. Considering the magnitude comparisons in Fig. 1 and the drift of orbital elements in Fig. 2, this work applies the second and the third order terms of the Earth's gravitational perturbation.

The equation of motion of a three-body system (with the Earth being the primary body and satellite the secondary body) is given by (Vallado, 2013, page 574)

$$\ddot{\vec{r}}_{\oplus sat} = -\frac{u_{\oplus}\vec{r}_{\oplus sat}}{r^3_{\oplus sat}} + u_3\left(\frac{\vec{r}_{sat3}}{r^3_{sat3}} - \frac{\vec{r}_{\oplus 3}}{r^3_{\oplus 3}}\right) \tag{5}$$

where u_3 is the gravitational parameter of the third-body. By expanding the $\frac{\vec{r}_{sat3}}{r^3_{sat3}}$ term in Eq. (5) using Legendre polynomials, Eq. (5) turns into (Vallado, 2013, pp. 575–576)

$$\ddot{\vec{r}}_{\oplus sat} = \underbrace{-\frac{u_{\oplus}\vec{r}_{\oplus sat}}{r^3_{\oplus sat}}}_{two-body\ \ acceleration} \underbrace{-u_3\left(\frac{-\vec{r}_{sat3}\left(3B+3B^2+B^3\right)+\vec{r}_{\oplus sat}}{r^3_{\oplus 3}}\right)}_{perturbative\ \ acceleration} \tag{6}$$

where

$$B = \sum_{j=1}^{\infty} P_j[\cos\varsigma]\left(\frac{r_{\oplus sat}}{r_{\oplus 3}}\right)^j \tag{7}$$

and ς is the angle between $\vec{r}_{\oplus 3}$ and $\vec{r}_{\oplus sat}$. Eq. (7) can be rewritten as

$$\begin{aligned} B &= B_1 + B_2 + B_3 + \cdots \\ B_j &= P_j[\cos\varsigma]\left(\frac{r_{\oplus sat}}{r_{\oplus 3}}\right)^j \end{aligned} \tag{8}$$

Taking the Sun and the Moon being the third body, it's obvious that $r_{\oplus sat} \ll r_{\oplus 3}$, which makes $|B_j| \ll 1$. So the $\left(3B^2+B^3\right)$ term in Eq. (6) is neglected when estimating the magnitude of acceleration caused by each B_j term in Eq. (8). Let's denote

$$\vec{A} = -u_3\frac{\vec{r}_{\oplus sat}}{r^3_{\oplus 3}}\vec{B}_i = u_3\frac{3\cdot\vec{r}_{sat3}B_i}{r^3_{\oplus 3}} \tag{9}$$

Varying ς from 0° to 180°, the magnitude of $\vec{A}$ and the maximal magnitudes of the $\vec{B}$ terms are calculated and presented for the Sun and the Moon respectively in Fig. 3. From Fig. 3(a) we see that, for the Sun, the magnitudes of $\vec{B}_1$ and $\vec{B}_2$ are comparable to that of SRP, while the magnitudes of the other $\vec{B}$ terms are at least 4 magnitudes smaller. It can be seen from Fig. 3(b) that, for the Moon, the magnitudes of the $\vec{B}_1$ to $\vec{B}_5$ terms are comparable to that of SRP.

Fig. 4 and Fig. 5 present the drift of orbital elements due to each $\vec{B}$ term for the Sun and the Moon respectively. From Fig. 4 one can find that, for the Sun, the semimajor axis and eccentricity drifts due to the $\vec{B}_j$ terms are bounded by 0.05 km and $2 \cdot 10^{-5}$ respectively, while the inclination drift caused by $\vec{B}_1$ is significant and reaches about 0.26 degrees. Situations are similar for the Moon. From Fig. 5 we see that, for the Moon, the semimajor axis and eccentricity drifts due to the $\vec{B}_j$ terms are bounded by 1.5 km and $9 \cdot 10^{-5}$ respectively, while the inclination drift caused by $\vec{B}_1$ reaches about 0.5 degrees.

Combining the magnitude comparisons in Fig. 3 and the drift of the orbital elements in Fig. 4 and Fig. 5, truncations of the third-body gravitational accelerations are made in the following manner. For the Sun, this work applies the $\vec{B}_1$ and $\vec{B}_2$ terms. For the Moon, the $\vec{B}_1, \vec{B}_2$ and $\vec{B}_3$ terms are considered when $A/M \geqslant 0.1$ kg/m^2, while the $\vec{B}_4$ and $\vec{B}_5$ terms are also taken into consideration when $A/M \geqslant 0.001$ kg/m^2.

The acceleration due to SRP for a perfectly reflecting solar sail is given by (McInnes, 1999, page 39)

$$\ddot{\vec{r}}_{\mathrm{SRP}} = \left(2P_{\odot}\frac{A}{m}\cos^2\alpha\right)\hat{\boldsymbol{n}} \tag{10}$$

where $P_{\odot}$ denotes magnitude of SRP. $P_{\odot}$ at 1 AU from the Sun equals to 4.56×10^{-6} N/m^2. A/m is the area to mass ratio of spacecraft, and α denotes the cone angle (the pitch angle in the 2D case) of the solar sail, which is the angle between the sail normal vector $\hat{\boldsymbol{n}}$ and the sun-line vector $\hat{\boldsymbol{u}}$.

A satellite in GEO experiences eclipse in the summer and winter. Only eclipse by the Earth is considered in this

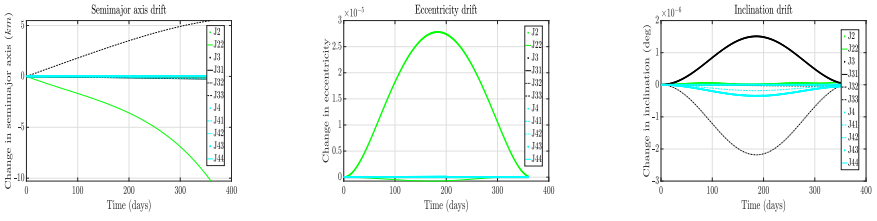

(a) Semi-major axis drift (b) Eccentricity drift (c) Inclination drift

Fig. 2. Drift of orbital elements due to different gravitational terms.

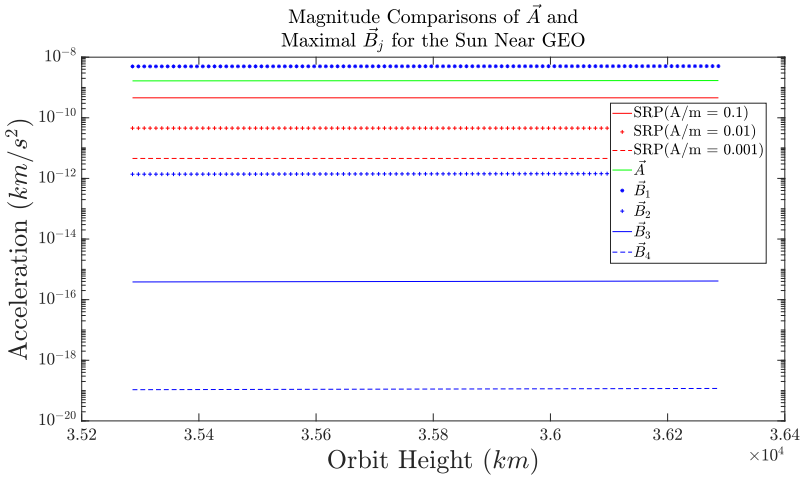

(a) Sun

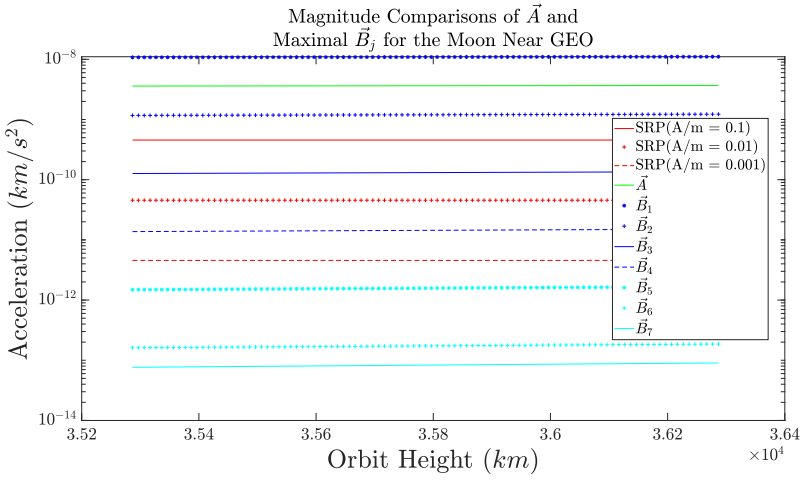

(b) Moon

Fig. 3. Magnitude comparisons of $\vec{A}$ and the maximal $\vec{B}_j$ near GEO.

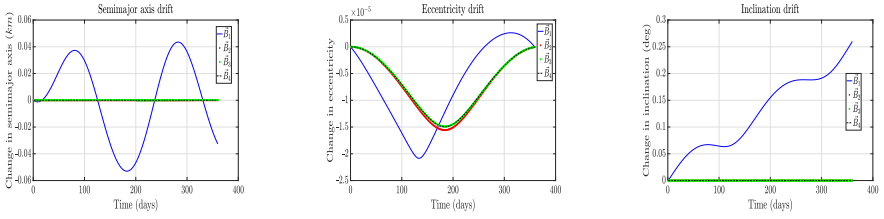

(a) Semi-major axis drift (b) Eccentricity drift (c) Inclination drift

Fig. 4. Drift of orbital elements due to different $\vec{B}_j$ terms for the sun.

work. Fig. 6 depicts the basic eclipse geometry. From the geometric relationships,

$$\begin{aligned} \sin\alpha_{umb} &= \frac{R_\odot - R_\oplus}{|\vec{r}_\odot|} \\ \sin\alpha_{pen} &= \frac{R_\odot + R_\oplus}{|\vec{r}_\odot|} \\ d_{EV} &= \frac{R_\oplus |\vec{r}_\odot|}{R_\odot - R_\oplus} \\ d_{EF} &= \frac{R_\oplus |\vec{r}_\odot|}{R_\odot + R_\oplus} \end{aligned} \tag{11}$$

where $R_\odot$ is the radius of the Sun, $R_\oplus$ the radius of the Earth, d_{EV} the distance from Earth to the vertex, and $\vec{r}_\odot$ denotes the Sun position vector in the Earth Centred Inertial (ECI) frame. Given the satellite position vector $\vec{r}_{sat}$ in the ECI frame, the angle between $\vec{r}_{sat}$ and $\vec{r}_\odot$ is

$$\epsilon_\odot = \arccos\left(\frac{\vec{r}_\odot \cdot \vec{r}_{sat}}{|\vec{r}_\odot||\vec{r}_{sat}|}\right) \tag{12}$$

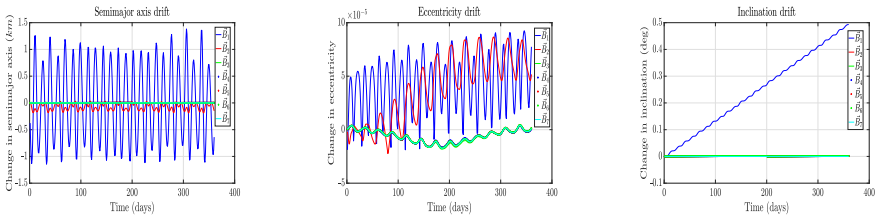

(a) Semi-major axis drift (b) Eccentricity drift (c) Inclination drift

Fig. 5. Drift of orbital elements due to different $\vec{\boldsymbol{B}}_j$ terms for the moon.

Let's denote

$$\begin{aligned} d_{satHor}(d_{DE}) &= -|\vec{\boldsymbol{r}}_{sat}| \cdot \cos\epsilon \\ d_{satVer}(d_{DG}) &= -|\vec{\boldsymbol{r}}_{sat}| \cdot \sin\epsilon \end{aligned} \tag{13}$$

Then the eclipse criterion can be given by

$$\begin{cases} d_{lenUmb}(d_{DM}) = (d_{EV} - d_{satHor}) \cdot \tan\alpha_{umb} \\ d_{lenPen}(d_{DN}) = (d_{EF} + d_{satHor}) \cdot \tan\alpha_{pen} \end{cases} \tag{14}$$

Thus, from geometry in Fig. 6, the eclipse conditions of satellite can be determined by

$$\begin{cases} \text{if} \quad d_{satVer} \geqslant d_{lenPen} & : \quad \text{No eclipse} \\ \text{if} \quad d_{satVer} \leqslant d_{lenUmb} & : \quad \text{In umbra} \\ \text{if} \quad \mathrm{d_{lenUmb}} < \mathrm{d_{satVer}} < \mathrm{d_{lenPen}} & : \quad \text{In penumbra} \end{cases} \tag{15}$$

For umbra, $P_{\odot umb} = 0\ \mathrm{N/m^2}$. For penumbra, $P_{\odot pen}$ equals to

$$P_{\odot pen} = P_{\odot} \cdot \frac{S_{\odot} - S_{Shadow}}{S_{\odot}} \tag{16}$$

where $S_{\odot}$ is the apparent area of the Sun looking from satellite, and S_{Shadow} denotes the area obscured by the Earth. This paper applies the cylindrical eclipse shadow model, from Fig. 7,

$$y(d_{JK}) = \frac{R_{\odot} \cdot x}{d_{lenPen} - d_{lenUmb}} \tag{17}$$

$$S_{Shadow}\left(S_{OPRQ} - S_{OPQ}\right) = \theta \cdot R_{\odot}^2 - R_{\odot}(R_{\odot} - y)\sin\theta \tag{18}$$

Combining Eq. (16), Eq. (17) and Eq. (18), SRP in penumbra can be calculated as

$$P_{\odot pen} = P_{\odot} \cdot \left(1 - \frac{\theta - (1 - y/R_{\odot})\sin\theta}{\pi}\right) \tag{19}$$

where

$$\theta = \arccos\left(\frac{R_{\odot} - y}{R_{\odot}}\right) \tag{20}$$

3. System modelling

3.1. Equations of motion

The time derivatives of the semimajor-axis (a), eccentricity (e) and inclination (i) are given by the Gauss's Variation of Parameter (VOP) equations (Vallado, 2013, Chap 7).

$$\frac{d}{dt}\begin{pmatrix} a \\ e \\ i \end{pmatrix} = \underbrace{\begin{pmatrix} \frac{2a^2}{\sqrt{ua(1-e^2)}} e\sin(\theta) & \frac{2a^2}{\sqrt{ua(1-e^2)}}(1 + e\cos(\theta)) & 0 \\ \sqrt{\frac{a(1-e^2)}{u}}\sin(\theta) & \sqrt{\frac{a(1-e^2)}{u}}\frac{2\cos(\theta) + e\left(1+\cos^2(\theta)\right)}{1+e\cos(\theta)} & 0 \\ 0 & 0 & \sqrt{\frac{a(1-e^2)}{u}}\frac{\cos(\omega+\theta)}{1+e\cos(\theta)} \end{pmatrix}}_{denote\ \boldsymbol{P}(a,e,i,t)} \begin{pmatrix} f_r \\ f_\theta \\ f_z \end{pmatrix} \tag{21}$$

Here f_r, f_θ, f_z denote perturbative forces in the Local-Vertical Local-Horizontal ($\boldsymbol{LVLH}$, denoted as $\boldsymbol{\mathcal{F}}_o$) frame, and θ is the true anomaly of spacecraft.

To express the acceleration due to SRP, a new frame $\boldsymbol{\mathcal{F}}_s$ is constructed. As depicted in Fig. 8 (a), axis $\hat{\boldsymbol{s}}_1$ is aligned with Sun-line vector (points from the Sun to satellite) $\hat{\boldsymbol{u}}$, axis $\hat{\boldsymbol{s}}_3$ lies in the plane constructed by $\hat{\boldsymbol{s}}_1$ and $\hat{\boldsymbol{g}}_3$ (with $\boldsymbol{\mathcal{F}}_g$ being the ECI frame) and being perpendicular to $\hat{\boldsymbol{s}}_1$, and axis $\hat{\boldsymbol{s}}_2$ completes the right hand rule. From Fig. 8 (a),

$$\begin{aligned} \hat{\boldsymbol{s}}_1 &= \hat{\boldsymbol{u}} \\ \hat{\boldsymbol{s}}_3 &= \frac{\hat{\boldsymbol{g}}_3 - (\hat{\boldsymbol{g}}_3 \cdot \hat{\boldsymbol{u}})\hat{\boldsymbol{u}}}{|\hat{\boldsymbol{g}}_3 - (\hat{\boldsymbol{g}}_3 \cdot \hat{\boldsymbol{u}})\hat{\boldsymbol{u}}|} \\ \hat{\boldsymbol{s}}_2 &= \hat{\boldsymbol{s}}_3 \times \hat{\boldsymbol{s}}_1 \end{aligned} \tag{22}$$

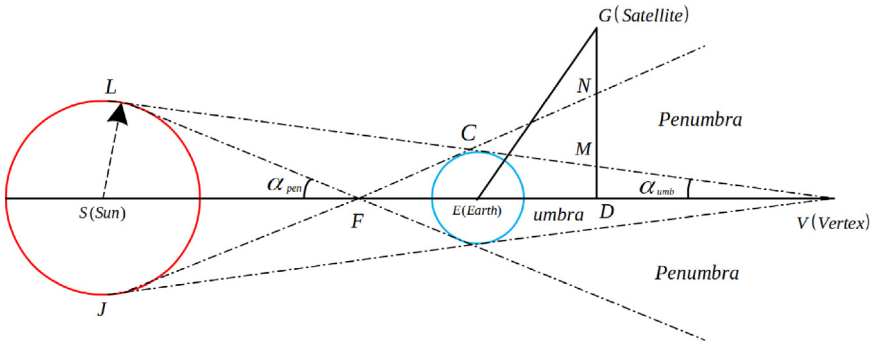

Fig. 6. Eclipse geometry.

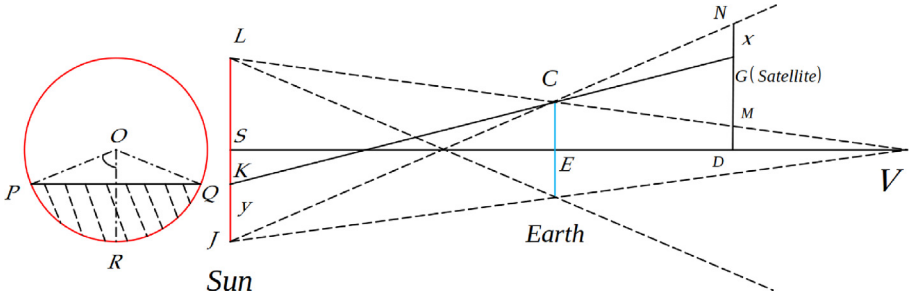

Fig. 7. Cylindrical eclipse shadow model.

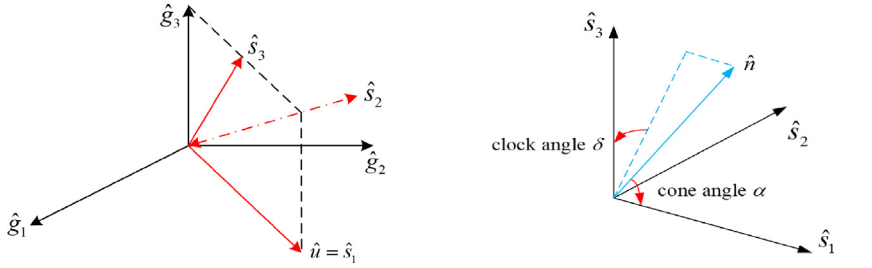

(a) The $\mathcal{F}_s$ Frame (b) Cone Angle and Clock Angle in $\mathcal{F}_s$

Fig. 8. Express SRP in the constructed frame $\mathcal{F}_s$.

The sail normal vector $\hat{\boldsymbol{n}}$ in $\mathcal{F}_s$ is given by Eq. (23), where α ($\in [0°, 90°]$) and δ ($\in [0°, 360°]$) are the cone angle and clock angle of the sail (Fig. 8 (b)). The rotation matrix from $\mathcal{F}_s$ to $\mathcal{F}_g$ is given by $\boldsymbol{C}_{GS} = \vec{\boldsymbol{f}}_g \cdot \vec{\boldsymbol{f}}_s^T$. Recall that the acceleration due to SRP for a perfectly reflecting sail is equal to $2P_\odot \cdot (A/m) \cdot \cos^2(\alpha) \cdot \hat{\boldsymbol{n}}$, so the acceleration due to SRP in $\mathcal{F}_o$ can be expressed using Eq. (24), where $\boldsymbol{C}_{OP} = \boldsymbol{C}_3(\theta), \boldsymbol{C}_{PG} = \boldsymbol{C}_3(\omega)\boldsymbol{C}_1(\theta)\boldsymbol{C}_3(\Omega)$ are rotation matrices from the Perifocal Coordinate Frame (denoted as $\mathcal{F}_p$) to $\mathcal{F}_o$ and from $\mathcal{F}_g$ to $\mathcal{F}_p$ respectively.

$$\hat{\boldsymbol{n}} = \begin{pmatrix} \cos\alpha \\ \sin(\alpha)\sin(\delta) \\ \sin(\alpha)\cos(\delta) \end{pmatrix} \tag{23}$$

$$\begin{pmatrix} f_r \\ f_\theta \\ f_z \end{pmatrix} = (\boldsymbol{C}_{OP}\boldsymbol{C}_{PG}\boldsymbol{C}_{GS} \cdot 2P_\odot \cdot A/m) \cdot \begin{pmatrix} \cos^3\alpha \\ \sin(\alpha)\cos^2(\alpha)\sin(\delta) \\ \sin(\alpha)\cos^2(\alpha)\cos(\delta) \end{pmatrix} \tag{24}$$

Substituting Eq. (24) into Eq. (21) yields

$$\begin{aligned} \underbrace{\frac{d}{dt}\begin{pmatrix} a \\ e \\ i \end{pmatrix}}_{\dot{\boldsymbol{x}}} &= \underbrace{\begin{pmatrix} f_1(a,e,i,\alpha,\delta,t) \\ f_2(a,e,i,\alpha,\delta,t) \\ f_3(a,e,i,\alpha,\delta,t) \end{pmatrix}}_{\boldsymbol{f}(\boldsymbol{x},\boldsymbol{u},t)} \\ &= 2P_\odot \cdot (A/m) \cdot \boldsymbol{P}(a,e,i,t) \\ &\quad \cdot \boldsymbol{C}_3(\theta)\boldsymbol{C}_3(\omega)\boldsymbol{C}_1(\theta)\boldsymbol{C}_3(\Omega)\boldsymbol{C}_{GS} \cdot \begin{pmatrix} \cos^3\alpha \\ \sin(\alpha)\cos^2(\alpha)\sin(\delta) \\ \sin(\alpha)\cos^2(\alpha)\cos(\delta) \end{pmatrix} \end{aligned} \tag{25}$$

This is a nonlinear and time-varying system, which can be controlled by α and δ. Eq. (24) and Eq. (25) also imply that when the cone angle α is set to 90°, the acceleration caused by SRP goes to zero, and the state will remain constant if no disturbance is considered.

3.2. Equilibrium analysis

Setting the derivatives in Eq. (25) to zero yields the following equilibrium points: $\alpha = \pi/2$ with no constraint on δ, a, e, i. It implies that, at the equilibrium condition, the sail is along the sun-line. This makes sense because in this situation the SRP exerted on the sail is zero, which makes it a two-body motion; thus the orbital elements remain constant. Linearizing Eq. (25) around the equilibria,

$$(\dot{\delta \boldsymbol{x}}) = \boldsymbol{A}_e(t)\delta\boldsymbol{x} + \boldsymbol{B}_e(t)\delta\boldsymbol{u} \tag{26}$$

we have $(\dot{\delta \boldsymbol{x}}) = \boldsymbol{0}$, where $\boldsymbol{A}_e(t) = \boldsymbol{B}_e(t) = 0$ are Jacobian matrices. This implies that the system is not controllable around the equilibrium points.

3.3. Linearization around a nominal trajectory

A nominal trajectory $\boldsymbol{x}_n(t)$ is created by prescribing control input $\boldsymbol{u}_n(t) = [\alpha_n(t), \delta_n(t)]^T$ and simulation time T. The choice of $\alpha_n(t)$ and $\delta_n(t)$ will be discussed later in Section 5. Along the nominal trajectory, only the control force (SRP) is considered. Disturbance forces (Earth gravitational perturbation and third-body perturbations) are to be accommodated later with proper control inputs. The system in Eq. (25) with disturbance is given by

$$\dot{\boldsymbol{x}}(t) = \boldsymbol{g}(\boldsymbol{x}, \boldsymbol{u}, \boldsymbol{d}, t) = \begin{pmatrix} f_1(\boldsymbol{x}, \boldsymbol{u}, t) \\ f_2(\boldsymbol{x}, \boldsymbol{u}, t) \\ f_3(\boldsymbol{x}, \boldsymbol{u}, t) \end{pmatrix} + \boldsymbol{d}(t) \tag{27}$$

where $\boldsymbol{d}(t) = \boldsymbol{P}(a, e, i, t)\boldsymbol{f}_d$ is the disturbance term, with $\boldsymbol{f}_d$ being the disturbance force vector expressed in $\mathcal{F}_o$. Linearizing the system around a nominal trajectory $\boldsymbol{x}_n(t)$ yields

$$(\dot{\delta \boldsymbol{x}}) = \underbrace{\frac{\partial \boldsymbol{g}}{\partial \boldsymbol{x}}[\boldsymbol{x}_n, \boldsymbol{u}_n, \boldsymbol{d}_n]_{A(t)}}\delta\boldsymbol{x} + \underbrace{\frac{\partial \boldsymbol{g}}{\partial \boldsymbol{u}}[\boldsymbol{x}_n, \boldsymbol{u}_n, \boldsymbol{d}_n]}_{\boldsymbol{B}(t)}\delta\boldsymbol{u} + \underbrace{\frac{\partial \boldsymbol{g}}{\partial \boldsymbol{d}}[\boldsymbol{x}_n, \boldsymbol{u}_n, \boldsymbol{d}_n]}_{\boldsymbol{d}(t)}\delta\boldsymbol{d} \tag{28}$$

where $\delta\boldsymbol{x} = \boldsymbol{x} - \boldsymbol{x}_n, \delta\boldsymbol{u} = \boldsymbol{u} - \boldsymbol{u}_n$ are deviations from the nominal trajectory and nominal control input. Along the nominal trajectory, $\boldsymbol{d}_n = \boldsymbol{0}$, so $\delta\boldsymbol{d} = \boldsymbol{d} - \boldsymbol{d}_n = \boldsymbol{d}$ is the actual disturbance. Define $\boldsymbol{X} \triangleq \delta\boldsymbol{x}, \boldsymbol{U} \triangleq \delta\boldsymbol{u}$, and note that $\frac{\partial \boldsymbol{g}}{\partial \boldsymbol{d}}[\boldsymbol{x}_n, \boldsymbol{u}_n, \boldsymbol{d}_n] = 1$, so Eq. (28) turns into

$$\dot{\boldsymbol{X}}(t) = \boldsymbol{A}(t)\boldsymbol{X}(t) + \boldsymbol{B}(t)\boldsymbol{U}(t) + \boldsymbol{d}(t) \tag{29}$$

This is a Linear Time Varying (LTV) system with a disturbance term, where $\boldsymbol{A}(t), \boldsymbol{B}(t), \boldsymbol{d}(t)$ are modelled along the nominal trajectory.

3.4. Equations of motion under an impulsive thrust

Consider the equations of motion with an impulsive thrust applied at time epoch t_k:

$$\dot{\boldsymbol{x}} = \boldsymbol{h}(\boldsymbol{x}, \boldsymbol{u}, \boldsymbol{d}) = \begin{pmatrix} f_1(\boldsymbol{x}, \boldsymbol{u}) \\ f_2(\boldsymbol{x}, \boldsymbol{u}) \\ f_3(\boldsymbol{x}, \boldsymbol{u}) \end{pmatrix} + \boldsymbol{d} + \underbrace{\boldsymbol{P}(\boldsymbol{x}, t)\boldsymbol{f}_t \cdot \delta(t - t_k)}_{thrusts} \tag{30}$$

where $\boldsymbol{f}_t$ is the thrust vector in $\mathcal{F}_o$. Note that the first two terms on the right hand side are continuous in time. So if we integrate Eq. (30) from time epoch t_k^- to t_k^+, we have

$$\int_{t_k^-}^{t_k^+} \dot{\boldsymbol{x}}(t)dt = \int_{t_k^-}^{t_k^+} \boldsymbol{P}(\boldsymbol{x}, t)\boldsymbol{f}_t \cdot \delta(t - t_k)dt \tag{31}$$

If the impulse is small, $\boldsymbol{P}(\boldsymbol{x}, t)$ remains constant. Also note that $\boldsymbol{X}_{t_k}^{\pm} = \boldsymbol{x}_{t_k}^{\pm} - \boldsymbol{x}_n(t_k)$, so Eq. (31) finally turns into

$$\boldsymbol{X}_{t_k}^{+} = \boldsymbol{X}_{t_k}^{-} + \boldsymbol{P}(t_k)\boldsymbol{f}_k \tag{32}$$

where $\boldsymbol{P}(t_k)$ denotes the $\boldsymbol{P}(\boldsymbol{x}, t)$ matrix at time epoch t_k, and $\boldsymbol{f}_k$ is the impulsive thrust applied at t_k in $\mathcal{F}_o$.

4. Optimal hybrid disturbance accommodation tracking control

When the A/M ratio of the spacecraft is small, impulsive thrusts are applied to assist the removal process. Consider the desired state in the GEO graveyard region $\boldsymbol{x}_d = [a_d, e_d, i_d]^T$. Recall that the states in the linearized system Eq. (29) $\boldsymbol{X}(t) = \boldsymbol{x}(t) - \boldsymbol{x}_n(t)$ are defined as the deviation of the true states $\boldsymbol{x}(t)$ from the nominal trajectory $\boldsymbol{x}_n(t)$. If $\boldsymbol{X}(t)$ in the linearized system tracks the desired trajectory $\boldsymbol{Z}(t)$ defined as $\boldsymbol{x}_d(t) - \boldsymbol{x}_n(t)$, then $\boldsymbol{x}(t) = \boldsymbol{x}_d(t)$, which is the desired situation. Therefore, it turns out to be a hybrid disturbance accommodation tracking problem.

Bryson (2018, Section 3) first proposed a variational approach for solving optimal control problems with discontinuities originating in the states. Vatankhahghadim and Damaren (Vatankhahghadim and Damaren, 2016b) extended the hybrid Linear Quadratic Regulator (LQR), which was originally developed by Sobiesiak and Damaren (Sobiesiak and Damaren, 2014), to a hybrid disturbance-accommodation LQR. The hybrid linear stability of a periodic system is analyzed in (Vatankhahghadim and Damaren, 2016a). (Vatankhahghadim and Damaren, 2016b) and (Vatankhahghadim and Damaren, 2016a) also studied the optimal impulse epochs, concluding that to target the impulses at the most uncontrollable parts of the continuous system, the impulses should be applied at the epochs when the smallest eigenvalue of the continuous system's controllability Gramian reaches a local minimum. Furthermore, the hybrid passivity theorem is developed in (Vatankhahghadim and Damaren, 2017b; Vatankhahghadim and Damaren, 2017a) presented a Cartesian relative motion approach to optimal formation

flight using the hybrid LQR. In this work, inspired by (Chun et al., 1985), the hybrid disturbance-accommodation LQR in (Vatankhahghadim and Damaren, 2016b) is extended to be capable of tracking a desired trajectory.

The continuous and discrete dynamic systems are given by Eq. (29) and Eq. (32) respectively:

$$\dot{\boldsymbol{x}}(t) = \boldsymbol{A}(t)\boldsymbol{x}(t) + \boldsymbol{B}(t)\boldsymbol{u}(t) + \boldsymbol{d}(t) \tag{33}$$

$$\boldsymbol{x}(t_k^+) = \boldsymbol{C}_k\boldsymbol{x}(t_k^-) + \boldsymbol{D}_k\boldsymbol{v}_k \tag{34}$$

where $k = 1, 2, \ldots, N-1$, represents $N-1$ impulse time epochs. The goal is to find the continuous and discrete control inputs $\boldsymbol{u}(t)$ and $\boldsymbol{v}_k$ that make the state $\boldsymbol{x}(t)$ track the desired trajectory $\boldsymbol{z}(t)$. Define the tracking error $\boldsymbol{e}(t) = \boldsymbol{x}(t) - \boldsymbol{z}(t)$. We seek to minimize the hybrid cost functional

$$\begin{aligned} J(\boldsymbol{x}(t), \boldsymbol{z}(t), \boldsymbol{u}(t), \boldsymbol{v}_k, t_k) = {} & \frac{1}{2}\boldsymbol{e}^T(t_f)\boldsymbol{S}\boldsymbol{e}(t_f) \\ & + \sum_{k=0}^{N-1}\int_{t_k^+}^{t_{k+1}^-}\left(\frac{1}{2}\boldsymbol{e}^T(t)\boldsymbol{Q}\boldsymbol{e}(t) + \frac{1}{2}\boldsymbol{u}^T(t)\boldsymbol{R}\boldsymbol{u}(t)\right)dt \\ & + \sum_{k=1}^{N-1}\left(\frac{1}{2}\boldsymbol{e}^T(t_k^-)\boldsymbol{Q}_k\boldsymbol{e}(t_k^-) + \frac{1}{2}\boldsymbol{v}_k^T\boldsymbol{R}_k\boldsymbol{v}_k\right) \end{aligned} \tag{35}$$

where $\boldsymbol{S} = \boldsymbol{S}^T \geqslant 0$ penalizes the final state, $\boldsymbol{Q} = \boldsymbol{Q}^T \geqslant 0, \boldsymbol{R} = \boldsymbol{R}^T > 0$ penalizes the continuous-time state and control inputs, and $\boldsymbol{Q}_k = \boldsymbol{Q}_k^T \geqslant 0, \boldsymbol{R}_k = \boldsymbol{R}_k^T > 0$ set the discrete-time state and control penalties. In addition, $t_0^+ = t_0$ and $t_N^- = t_f$. The continuous and discrete Hamiltonians are defined as

$$\begin{aligned} H_c(\boldsymbol{x}(t), \boldsymbol{z}(t), \boldsymbol{u}(t)) = {} & \frac{1}{2}\boldsymbol{e}^T(t)\boldsymbol{Q}\boldsymbol{e}(t) + \frac{1}{2}\boldsymbol{u}^T(t)\boldsymbol{R}\boldsymbol{u}(t) \\ & + \boldsymbol{\lambda}^T(t)(\boldsymbol{A}(t)\boldsymbol{x}(t) + \boldsymbol{B}(t)\boldsymbol{u}(t) + \boldsymbol{d}(t)) \end{aligned} \tag{36}$$

$$\begin{aligned} H_d(\boldsymbol{x}(t), \boldsymbol{z}(t), \boldsymbol{v}_k) = {} & \frac{1}{2}\boldsymbol{e}^T(t_k^-)\boldsymbol{Q}_k\boldsymbol{e}(t_k^-) + \frac{1}{2}\boldsymbol{v}_k^T\boldsymbol{R}_k\boldsymbol{v}_k \\ & + \nu_k^T(\boldsymbol{C}_k\boldsymbol{x}(t_k^-) + \boldsymbol{D}_k\boldsymbol{v}_k) \end{aligned} \tag{37}$$

where $\boldsymbol{\lambda}(t)$ and ν_k are Lagrange multipliers (also called the co-states of the hybrid system). Taking the first variation of J and setting it to zero yields the following optimal conditions:

$$\frac{\partial H_c}{\partial \boldsymbol{u}(t)} = 0 \tag{38}$$

$$\frac{\partial H_d}{\partial \boldsymbol{v}_k} = 0 \tag{39}$$

$$-\dot{\boldsymbol{\lambda}} = \frac{\partial H_c}{\partial \boldsymbol{x}(t)} = \boldsymbol{Q}\boldsymbol{e}(t) + \boldsymbol{A}^T(t)\boldsymbol{\lambda} \tag{40}$$

$$\boldsymbol{\lambda}(t_k^-) = \frac{\partial H_d}{\partial \boldsymbol{x}(t_k^-)} = \boldsymbol{Q}_k\boldsymbol{e}(t_k^-) + \boldsymbol{C}_k^T\nu_k \tag{41}$$

with boundary conditions:

$$\boldsymbol{\lambda}(t_f) = \boldsymbol{S}\boldsymbol{e}(t_f) \tag{42}$$

$$\boldsymbol{\lambda}(t_k^+) = \nu_k \tag{43}$$

4.1. Optimal continuous-time control input

From Eq. (38), Eq. (40) and Eq. (33), the closed-loop continuous system is given by

$$\dot{\boldsymbol{x}}(t) = \boldsymbol{A}(t)\boldsymbol{x}(t) - \boldsymbol{B}(t)\boldsymbol{R}^{-1}\boldsymbol{B}^T(t)\boldsymbol{\lambda}(t) + \boldsymbol{d}(t) \tag{44}$$

$$\dot{\boldsymbol{\lambda}}(t) = -\boldsymbol{Q}\boldsymbol{x}(t) - \boldsymbol{A}^T(t)\boldsymbol{\lambda}(t) + \boldsymbol{Q}\boldsymbol{z}(t) \tag{45}$$

Inspired by Athans and Falb (2013, Chap 9) and Chun et al. (1985), the solution of $\boldsymbol{\lambda}(t)$ is in the form $\boldsymbol{\lambda}(t) = \boldsymbol{P}(t)\boldsymbol{x}(t) - \boldsymbol{g}(t)$. Taking the time derivative of $\boldsymbol{\lambda}(t)$ and combining Eq. (44) and Eq. (45), one can find

$$\begin{aligned} & \left(-\boldsymbol{Q} - \boldsymbol{A}^T(t)\boldsymbol{P}(t) - \boldsymbol{P}(t)\boldsymbol{A}(t) - \dot{\boldsymbol{P}}(t) + \boldsymbol{P}(t)\boldsymbol{B}(t)\boldsymbol{R}^{-1}\boldsymbol{B}^T(t)\boldsymbol{P}(t)\right)\cdot \\ & \boldsymbol{x}(t) = -\boldsymbol{Q}\boldsymbol{z}(t) - \left(\boldsymbol{A}^T(t) - \boldsymbol{P}(t)\boldsymbol{B}(t)\boldsymbol{R}^{-1}\boldsymbol{B}^T(t)\right)\boldsymbol{g}(t) \\ & \quad + \boldsymbol{P}(t)\boldsymbol{d}(t) - \dot{\boldsymbol{g}}(t) \end{aligned} \tag{46}$$

For this to hold for all $\boldsymbol{x}(t)$, both sides should be zero. Therefore,

$$\begin{aligned} \dot{\boldsymbol{P}}(t) = {} & -\boldsymbol{Q} - \boldsymbol{A}^T(t)\boldsymbol{P}(t) - \boldsymbol{P}(t)\boldsymbol{A}(t) \\ & + \boldsymbol{P}(t)\boldsymbol{B}(t)\boldsymbol{R}^{-1}\boldsymbol{B}^T(t)\boldsymbol{P}(t) \end{aligned} \tag{47}$$

$$\dot{\boldsymbol{g}}(t) = -\boldsymbol{Q}\boldsymbol{z}(t) - \left(\boldsymbol{A}^T(t) - \boldsymbol{P}(t)\boldsymbol{B}(t)\boldsymbol{R}^{-1}\boldsymbol{B}^T(t)\right)\boldsymbol{g}(t) + \boldsymbol{P}(t)\boldsymbol{d}(t) \tag{48}$$

By comparing $\boldsymbol{\lambda}(t) = \boldsymbol{P}(t)\boldsymbol{x}(t) - \boldsymbol{g}(t)$ with Eq. (42), one can find the boundary conditions

$$\boldsymbol{P}(t_f) = \boldsymbol{S} \tag{49}$$

$$\boldsymbol{g}(t_f) = \boldsymbol{S}\boldsymbol{z}(t_f) \tag{50}$$

At last, using Eq. (38) the optimal control law of the continuous-time system can be given by

$$\boldsymbol{u}^*(t) = -\boldsymbol{R}^{-1}\boldsymbol{B}^T(t)(\boldsymbol{P}(t)\boldsymbol{x}(t) - \boldsymbol{g}(t)) \tag{51}$$

where $\boldsymbol{P}(t)$ and $\boldsymbol{g}(t)$ can be calculated by integrating Eq. (47) and Eq. (48) simultaneously backwards, using boundary conditions in Eq. (49) and Eq. (50). This result coincides with (Chun et al., 1985, Eqs. (8), (9) and (10)).

4.2. Optimal discrete-time control input

Once an impulse is reached, both the state and co-states experience discontinuities. Before and after an impulse, $\boldsymbol{\lambda}(t_k^{\pm}) = \boldsymbol{P}(t_k^{\pm})\boldsymbol{x}(t_k^{\pm}) - \boldsymbol{g}(t_k^{\pm})$. Using the optimal and boundary conditions in Eq. (43) and Eq. (41), the closed-loop discrete dynamics are obtained for $\boldsymbol{x}(t_k^+)$; rearranging which for $\boldsymbol{x}(t_k^-)$ and using $\boldsymbol{x}(t_k^+) = \boldsymbol{P}^{-1}(t_k^+)(\boldsymbol{\lambda}(t_k^+) + \boldsymbol{g}(t_k^+))$ yields

$$\begin{aligned} \boldsymbol{x}(t_k^-) = {} & \boldsymbol{C}_k^{-1}\underbrace{\left(\boldsymbol{P}^{-1}(t_k^+) + \boldsymbol{D}_k\boldsymbol{R}_k^{-1}\boldsymbol{D}_k^T\right)}_{\text{denote } \boldsymbol{S}_k}\boldsymbol{\lambda}(t_k^+) \\ & + \boldsymbol{C}_k^{-1}\boldsymbol{P}^{-1}(t_k^+)\boldsymbol{g}(t_k^+) \end{aligned} \tag{52}$$

Thus the closed-loop discrete system can be given by

$$\begin{pmatrix} \boldsymbol{x}(t_k^-) \\ \boldsymbol{\lambda}(t_k^-) \end{pmatrix} = \begin{pmatrix} 0 & \boldsymbol{C}_k^{-1}\boldsymbol{S}_k \\ 0 & \boldsymbol{Q}_k\boldsymbol{C}_k^{-1}\boldsymbol{S}_k + \boldsymbol{C}_k^T \end{pmatrix} \begin{pmatrix} \boldsymbol{x}(t_k^+) \\ \boldsymbol{\lambda}(t_k^+) \end{pmatrix} + \begin{pmatrix} \boldsymbol{C}_k^{-1}\boldsymbol{P}^{-1}(t_k^+)\boldsymbol{g}(t_k^+) \\ \boldsymbol{Q}_k\boldsymbol{C}_k^{-1}\boldsymbol{P}^{-1}(t_k^+)\boldsymbol{g}(t_k^+) - \boldsymbol{Q}_k\boldsymbol{z}(t_k) \end{pmatrix} \tag{53}$$

Solving $\boldsymbol{\lambda}(t_k^+)$ using Eq. (53), and combining the above closed-loop discrete system, one can obtain

$$\boldsymbol{\lambda}(t_k^-) = (\boldsymbol{Q}_k + \boldsymbol{C}_k^T\boldsymbol{S}_k^{-1}\boldsymbol{C}_k)\boldsymbol{x}(t_k^-) - \boldsymbol{C}_k^T\boldsymbol{S}_k^{-1}\boldsymbol{P}^{-1}(t_k^+)\boldsymbol{g}(t_k^+) - \boldsymbol{Q}_k\boldsymbol{z}(t_k) \tag{54}$$

which should coincide with $\boldsymbol{x}(t_k^-) = \boldsymbol{P}^{-1}(t_k^-)(\boldsymbol{\lambda}(t_k^-) + \boldsymbol{g}(t_k^-))$. Hence, the solution for the discrete co-states are

$$\boldsymbol{P}(t_k^-) = \boldsymbol{Q}_k + \boldsymbol{C}_k^T\boldsymbol{S}_k^{-1}\boldsymbol{C}_k \tag{55}$$

$$\boldsymbol{g}(t_k^-) = \boldsymbol{C}_k^T\boldsymbol{S}_k^{-1}\boldsymbol{P}^{-1}(t_k^+)\boldsymbol{g}(t_k^+) + \boldsymbol{Q}_k\boldsymbol{z}(t_k) \tag{56}$$

This means that $\boldsymbol{P}(t)$ and $\boldsymbol{g}(t)$ will experience discontinuities at impulse time epochs. To solve $\boldsymbol{P}(t)$ and $\boldsymbol{g}(t)$, Eq. (47), Eq. (48) and Eq. (55), Eq. (56) must be used in concert. This means that starting from the "initial" (terminal) condition $\boldsymbol{P}(t_f) = \boldsymbol{S}$ and $\boldsymbol{g}(t_f) = \boldsymbol{S}\boldsymbol{z}(t_f)$, $\dot{\boldsymbol{P}}(t)$ and $\dot{\boldsymbol{g}}(t)$ are integrated backward using Eq. (47) and Eq. (48) from t_f to t_{N-1}^+. At $t = t_{N-1}^+$, integration stops; $\boldsymbol{P}(t_{N-1}^-)$ and $\boldsymbol{g}(t_{N-1}^-)$ are calculated using Eq. (55) and Eq. (56). Then $\boldsymbol{P}(t_{N-1}^-)$ and $\boldsymbol{g}(t_{N-1}^-)$ are used as the new initial conditions for time period from t_{N-1}^- to t_{N-2}^+, and so on so forth. At last, using Eq. (39), the optimal discrete control input can be obtained as

$$\boldsymbol{v}_k^* = -\boldsymbol{R}_k^{-1}\boldsymbol{D}_k^T\boldsymbol{C}_k^{-T}\left((\boldsymbol{P}(t_k^-) - \boldsymbol{Q}_k)\boldsymbol{x}(t_k^-) - \boldsymbol{g}(t_k^-) + \boldsymbol{Q}_k\boldsymbol{z}(t_k)\right) \tag{57}$$

This result coincides with (Vatankhahghadim and Damaren, 2016b, Eqs. (17) and (18)) if the tracking term $\boldsymbol{z}(t_k)$ is set to zero.

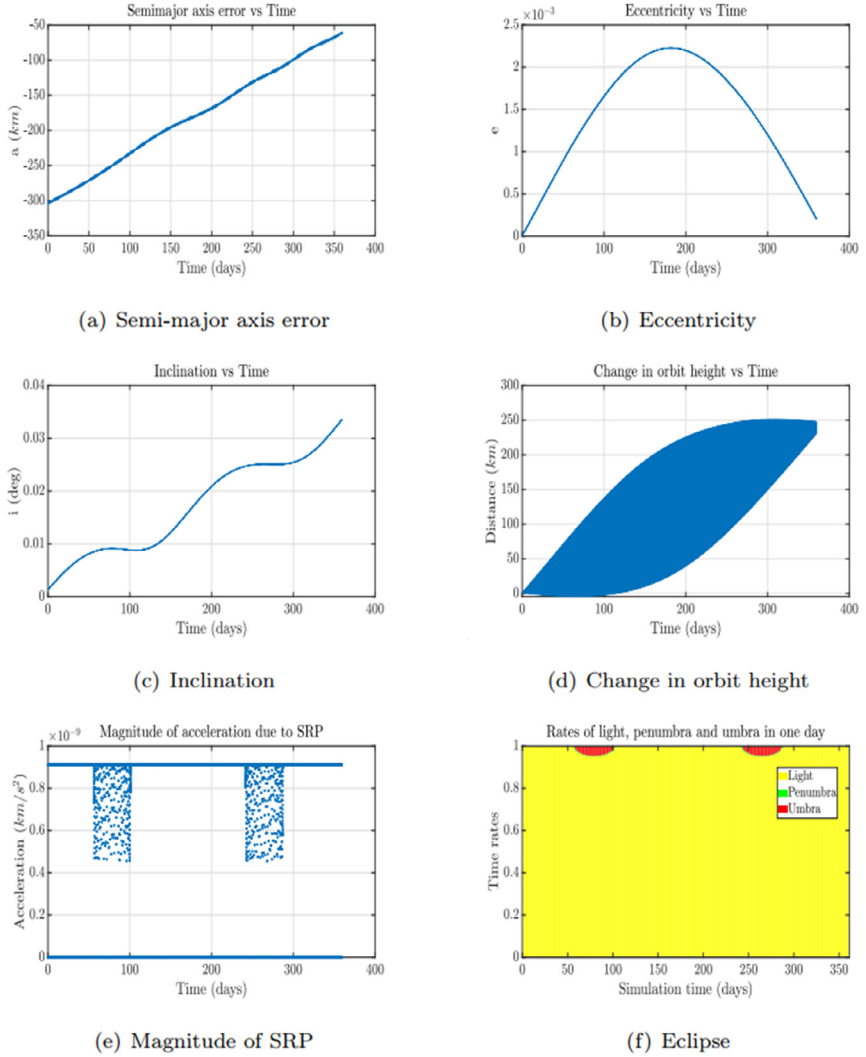

(a) Semi-major axis error

(b) Eccentricity

(c) Inclination

(d) Change in orbit height

(e) Magnitude of SRP

(f) Eclipse

Fig. 9. Nominal trajectory ($\alpha = 0°/90°, \delta = 180°$, A/M = 0.1 m^2/kg, 360 days).

5. Simulations

The initial position of the satellite in the ECI frame is arbitrarily selected as [0.0 km, 42164.5 km, 1.0 km]. The initial time is Jan 1st, 2017, 00:00:00, with the time constants $\Delta UT(UT1-UTC)=0.359485\text{s}, \Delta\text{AT}(\text{TAI}-\text{UTC})=37.0\text{s}$ (IERS, 2019). The time step of the simulations is 30 s. Because the orbit period of the Earth orbiting the Sun is about 1 year, in order to minimize the effect of SRP on increasing eccentricity, the simulation time is set to be 360 days. To avoid singularity in the orbital elements, the desired state is set to be $\boldsymbol{x}_d=[a_d,e_d,i_d]^T=[42164.5+300\,\text{km},10^{-6},10^{-6}]^T$.

5.1. Removing GEO satellites using only SRP

When impulsive thrusts are not involved, the state and control are both continuous in time. The solution of this

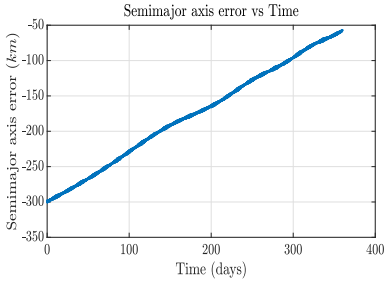

(a) Semi-major axis error

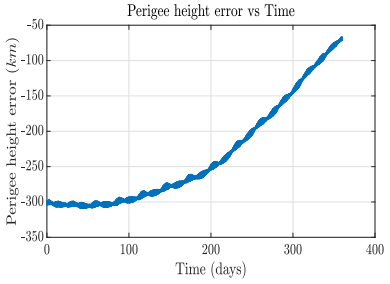

(b) Perigee error

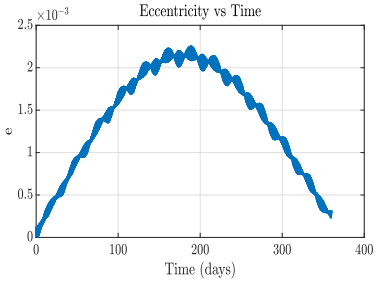

(c) Eccentricity

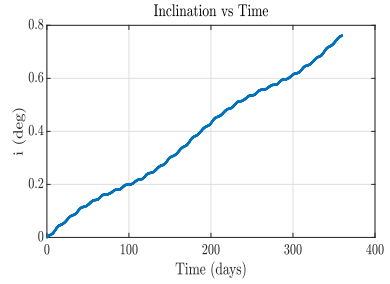

(d) Inclination

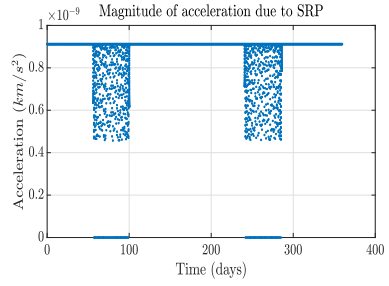

(e) Magnitude of SRP

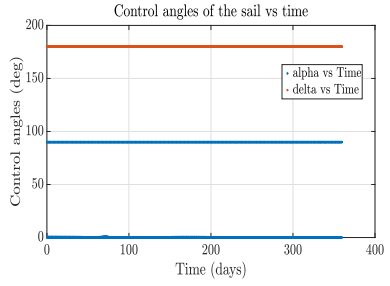

(f) Control angles of the sail

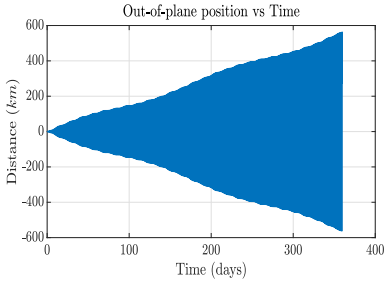

(g) Out of plane position

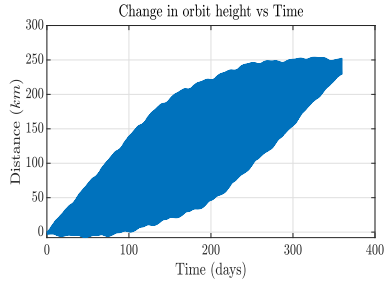

(h) Change in orbit height

Fig. 10. Actual trajectory ($\alpha=0°/90°, \delta=180°$, A/M = 0.1 m^2/kg, 360 days).

Table 3
Simulation results ($\alpha = 0°/90°$, various δ, A/M = 0.1 m^2/kg, 360 days)

Nominal α	Nominal δ	Final a error (km)	Final e error	Actual α	Actual δ
0°/90°	0°	−57.63	$-0.69 \cdot 10^{-3}$	[0°, 90°]	0°
	45°	−57.41	$-0.69 \cdot 10^{-3}$	[0°, 90°]	45°
	90°	−57.30	$-0.69 \cdot 10^{-3}$	[0°, 90°]	90°
	135°	−57.41	$-0.69 \cdot 10^{-3}$	[0°, 90°]	135°
	180°	−57.69	$-0.70 \cdot 10^{-3}$	[0°, 90°]	180°
	225°	−57.31	$-0.69 \cdot 10^{-3}$	[0°, 90°]	225°
	270°	−57.21	$-0.69 \cdot 10^{-3}$	[0°, 90°]	270°
	315°	−57.30	$-0.69 \cdot 10^{-3}$	[0°, 90°]	315°

continuous-time disturbance-accommodation tracking problem is given in Section 4.1. The system in Eq. (27) is linearized along three different sets of nominal trajectories.

(a) Set 1, $\alpha = 0°/90°, \delta = 180°$, A/M $= 0.1$ m^2/kgTo maximize the effect of SRP on increasing orbit height, the first nominal trajectory is created by setting $\alpha = 0°$ (sail normal vector is aligned with Sun-line vector, so SRP is maximized) when the sail is moving away from the Sun, $\alpha = 90°$ (sail normal vector is perpendicular to Sun-line vector, so SRP is turned off) when moving forward, and $\delta = 180°$ all the time. Nominal trajectories (the error from the desired orbital elements) are presented in Fig. 9.After some trial and error, the penalty matrices are set to $\boldsymbol{S} = \text{diag}[1, 1000, 0.5] \cdot 10^5, \boldsymbol{Q} = \boldsymbol{I}_3, \boldsymbol{R} = \boldsymbol{I}_2 \cdot 10^6$. After obtaining the optimal control $\boldsymbol{u}^*(t)$ (which is the deviation from $\boldsymbol{u}_n(t)$) from Eq. (51), the actual control input $\boldsymbol{u}(t) = \boldsymbol{u}^*(t) + \boldsymbol{u}_n(t)$. Simulation results are presented in Fig. 10.From Fig. 10 one can see that (1) the final semimajor-axis (perigee altitude) is about 60 (70) km below the desired one, (2) the final eccentricity is within the desired range ([-0.003,0.003]), (3) the orbit inclination grows very large due to the third-body gravitational accelerations, (4) the orbit height increases gradually, (5) there exist two periods of eclipse during the removal process, (6) the cone angle α varies within $[0°, 90°]$, while the clock angle δ remains 180°.Varying δ from 0° to 360°, simulation results are present in Table 3. From Table 3 we see that the angle δ remains at the initial value in all sets of simulations. This is because in the linearization, the elements of the second column of $\boldsymbol{B}(t)$ matrix in Eq. (29) all contain the term $\sin\alpha\cos^2\alpha$. Therefore, if α in nominal trajectory is chosen to be $0°/90°, \delta$ loses control authority.

(b) Set 2, $\alpha = 10°/80°$, various δ, A/M $= 0.1$ m^2/kgIn this set of nominal trajectory, $\alpha = 10°$ when the sail is moving away from the Sun, $\alpha = 80°$ when moving forward, $\delta = 180°$ all the time. Since $\sin\alpha\cos^2\alpha \neq 0$, the control authority of δ is guaranteed. The simulation results are shown in Fig. 11. Varying δ from 45° to 315°, the simulation results are presented in Table 4.From Fig. 11 and Table 4 we conclude that (1) the final semimajor-axis (perigee altitude) is about 70 (80) km below the desired one (which is worse than in set 1), (2) the final eccentricity is within the desired range ([−0.003,0.003]), (3) the orbit inclination grows very large due to the third-body gravitational accelerations, (4) the out-of-plane position and the orbit height increase gradually during the removal process, (5) the control authorities of α and δ are both guaranteed, (6) there exists one period of eclipse. The control authority of the cone angle δ is achieved at the cost of lowering the removing performance since the final semimajor axis is lower than in set 1 and the final eccentricity shows almost no difference. These sets of simulations imply that to remove end-of-life GEO satellites to the GEO graveyard region, a relatively larger A/M is required.

(c) Set 3, $\alpha = 0°/90°$, various δ, A/M $= 0.13$ m^2/kgWe gradually increase the A/M of spacecraft and find that, to remove GEO satellites to the GEO graveyard orbits in 360 days, the smallest A/M ratio required is about 0.13 m^2/kg. Simulation results are given in Fig. 12 and Table 5. From Fig. 12 and Table 5 we see that (1) the final semimajor-axis is about 13 km above the desired one, (2) the final perigee is just at the desired altitude, (3) the final eccentricity is within the desired range ([-0.003,0.003]), (4) the orbit inclination grows very large due to the third-body gravitational accelerations, (5) the out-of-plane position and the orbit height increase gradually during the removal process. With the A/M of 0.13 m^2/kg, the debris is successfully removed from GEO to the GEO graveyard region using only SRP.From Fig. 12, we can also find that there exists tracking errors at the final state. This undesired tracking error results from the inaccuracy of the linearized system. Because the simulation time is very long, the real-time trajectory tends to deviate from the nominal trajectory, which makes the linearized system "inaccurate" to some extent. However, by judiciously choosing the penalty matrices in Eq. (35), we can still achieve debris removal to the GEO graveyard region in the presence of the system inaccuracy.

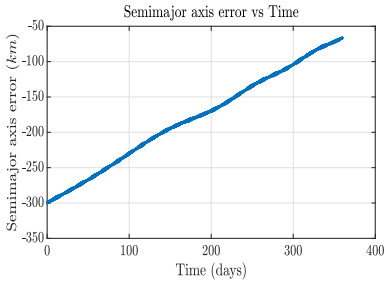

(a) Semi-major axis error

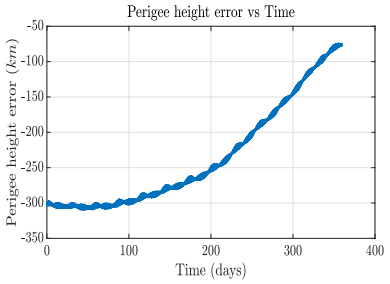

(b) Perigee error

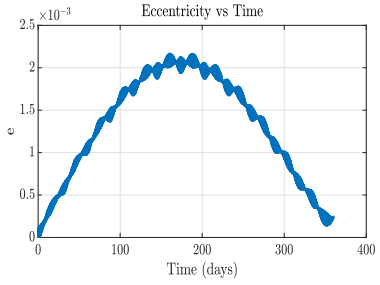

(c) Eccentricity

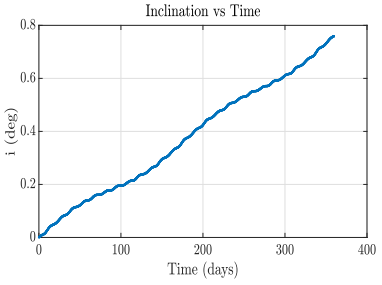

(d) Inclination

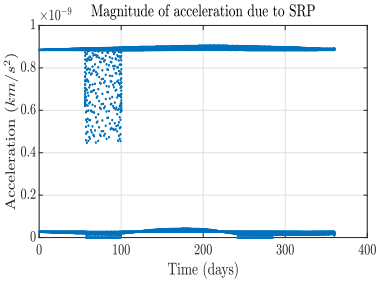

(e) Magnitude of SRP

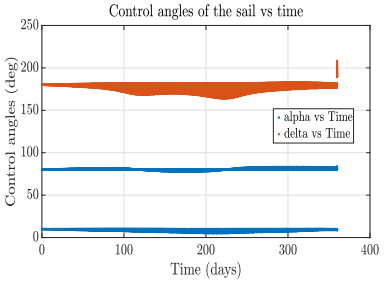

(f) Control angles

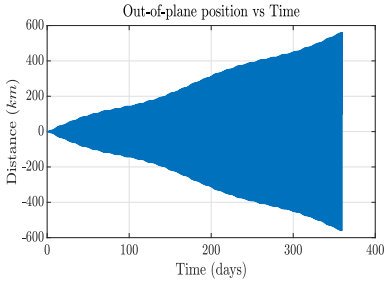

(g) Out of plane position

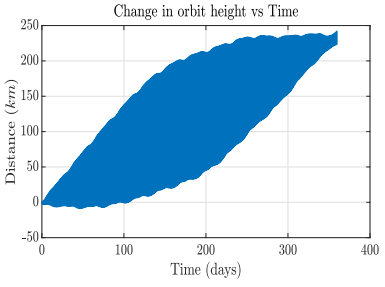

(h) Change in orbit height

Fig. 11. Actual trajectory ($\alpha = 10°/80°, \delta = 180°$, A/M $= 0.1$ m^2/kg, 360 days).

Table 4
Simulation results ($\alpha = 10°/80°$, various δ, A/M $= 0.1$ m^2/kg, 360 days)

Nominal α	Nominal δ	Final a error (km)	Final e error	Actual α	Actual δ
10°/80°	45°	−71.65	$-0.59 \cdot 10^{-3}$	[0°, 90°]	[44°, 47°]
	90°	−74.30	$-0.69 \cdot 10^{-3}$	[0°, 90°]	[89°, 91°]
	135°	−75.17	$-0.77 \cdot 10^{-3}$	[0°, 90°]	[129°, 138°]
	180°	−66.74	$-0.76 \cdot 10^{-3}$	[0°, 90°]	[164°, 183°]
	225°	−65.20	$-0.75 \cdot 10^{-3}$	[0°, 90°]	[220°, 230°]
	270°	−61.61	$-0.70 \cdot 10^{-3}$	[0°, 90°]	[269°, 271°]
	315°	−63.05	$-0.57 \cdot 10^{-3}$	[0°, 90°]	[313°, 318°]

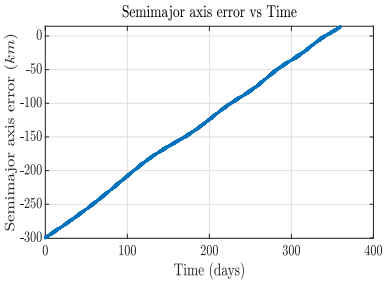

(a) Semi-major axis error

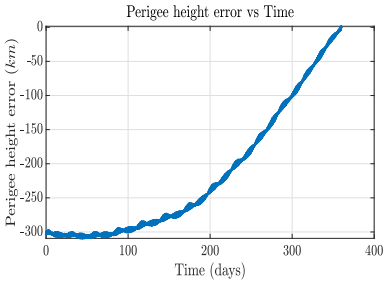

(b) Perigee Error

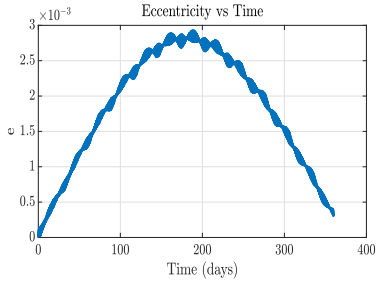

(c) Eccentricity error

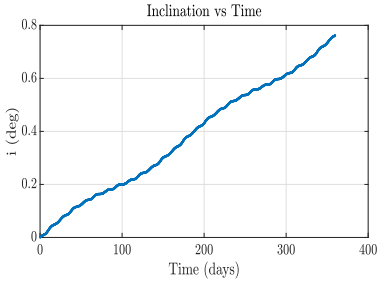

(d) Inclination error

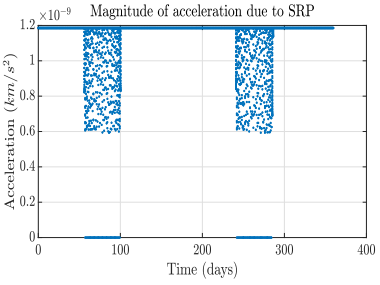

(e) Magnitude of SRP

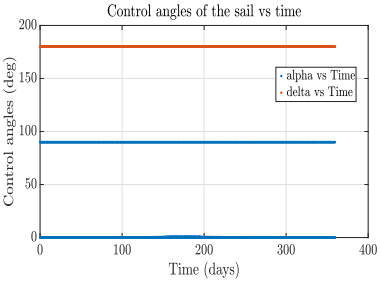

(f) Control angles

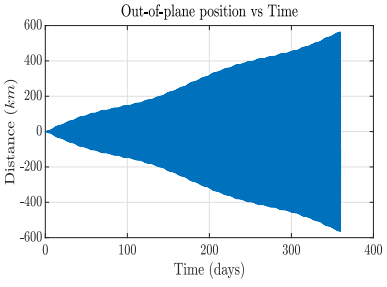

(g) Out of plane position

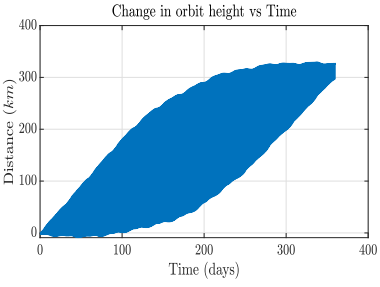

(h) Change in orbit height

Fig. 12. Actual trajectory ($\alpha = 0°/90°, \delta = 180°$, A/M $= 0.13$ m^2/kg, 360 days).

Table 5
Simulation results ($\alpha = 0°/90°$, various δ, A/M $= 0.13$ m^2/kg, 360 days)

Nominal α	Nominal δ	Final a error (km)	Final e error	Actual α	Actual δ
0°/90°	90°	+13.56	$-0.66 * 10^{-3}$	[0°, 90°]	90°
	180°	+13.43	$-0.67 * 10^{-3}$	[0°, 90°]	180°
	270°	+13.61	$-0.66 * 10^{-3}$	[0°, 90°]	270°

5.2. Removing GEO satellites using SRP and impulsive thrusts

When impulsive thrusts are applied, the state and control experience discontinuities at impulse epochs. The solution of this hybrid disturbance-accommodation tracking problem is given in Section 5. As in Section. 5.1, to maximize the effect of SRP on increasing orbit height, the nominal trajectory is created by setting $\alpha = 0^\circ$ (the sail normal vector is aligned with the Sun-line vector, so SRP is maximized) when the sail is moving away from the Sun, $\alpha = 90^\circ$ (the sail normal vector is perpendicular to the Sun-line vector, so SRP is turned off) when moving forward, and $\delta = 180^\circ$ all the time. The A/M of spacecraft is 0.1 m^2/kg. It's shown in Section 5.1 that when A/M is equal to 0.1 m^2/kg, debris can't be removed to the GEO graveyard region using only SRP, so here impulsive thrusts are applied to assist the removal process.

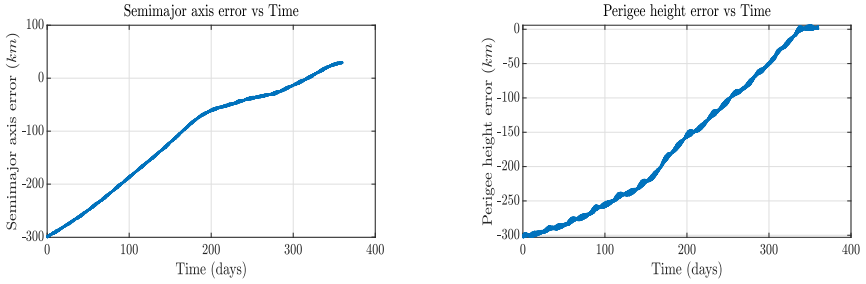

(a) Semi-major axis error

(b) Perigee Error

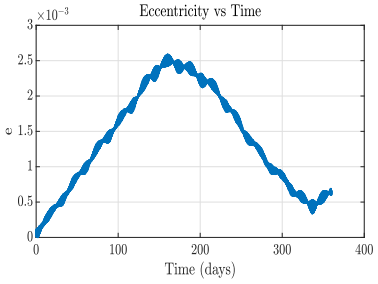

(c) Eccentricity error

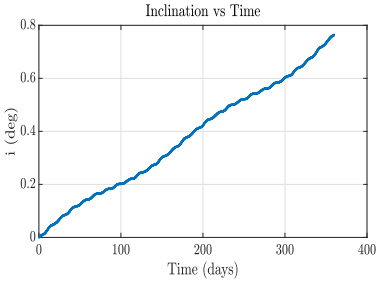

(d) Inclination error

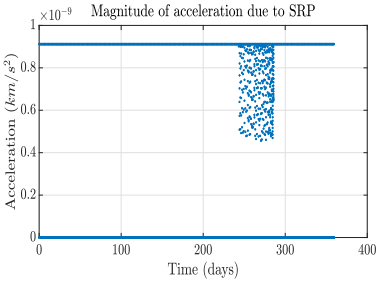

(e) Magnitude of SRP

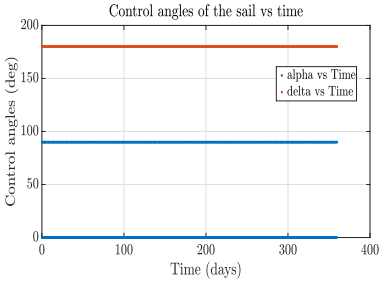

(f) Control angles

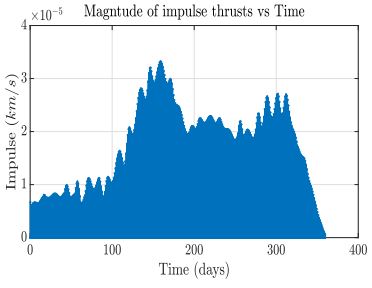

(g) Magnitude of impulsive thrusts

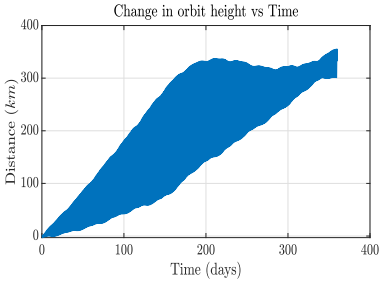

(h) Change in orbit height

Fig. 13. Actual trajectory (Hybrid control, $\alpha = 0^\circ/90^\circ, \delta = 180^\circ$, A/M $= 0.1$ m^2/kg, 360 days).

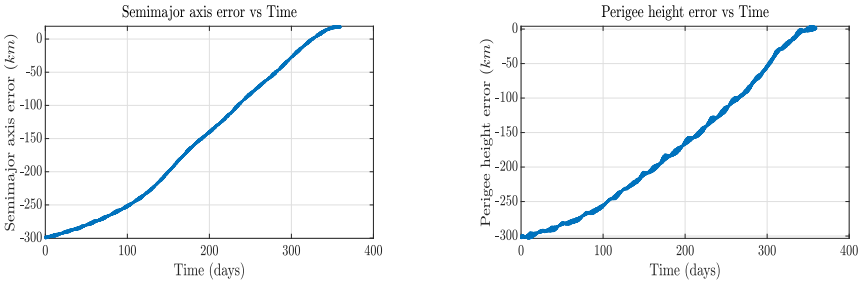

(a) Semi-major axis error

(b) Perigee Error

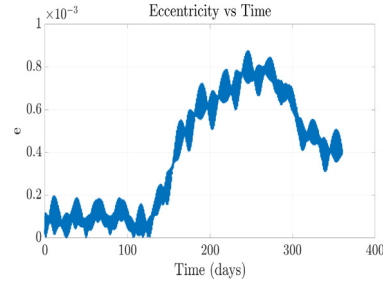

(c) Eccentricity error

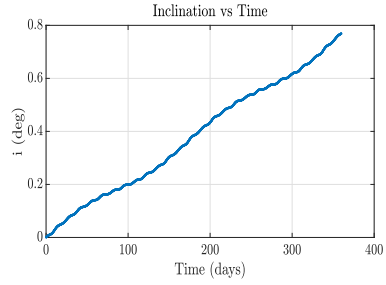

(d) Inclination error

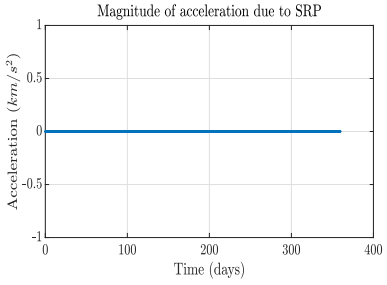

(e) Magnitude of SRP

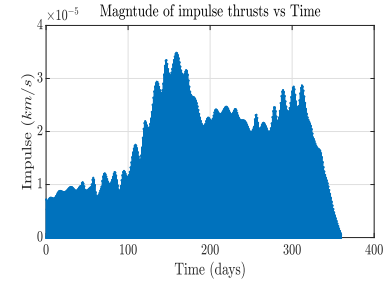

(f) Magnitude of impulsive thrusts

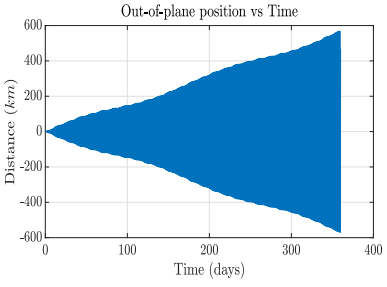

(g) Control angles

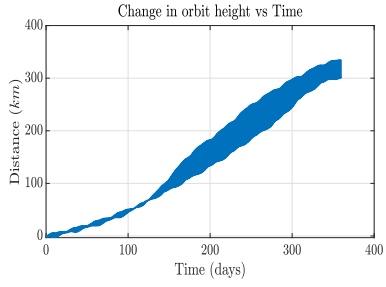

(h) Change in orbit height

Fig. 14. Actual trajectory (Impulsive thrusts, $\alpha = 0°/90°, \delta = 180°$, A/M $= 0.1$ m^2/kg, 360 days).

After some trial and error, the penalty matrices are set as $\boldsymbol{S} = \mathrm{diag}\left[25, 10^{10}, 1\right] \cdot 10^{10}, \boldsymbol{Q} = \mathrm{diag}\ \left[25, 10^{10}, 1\right] \cdot 10^{5}$, $\boldsymbol{R} = \boldsymbol{I}_2 \cdot 10^{20}, \boldsymbol{Q}_{\mathrm{k}} = \boldsymbol{I}_3, \boldsymbol{R}_{\mathrm{k}} = \boldsymbol{I}_3 \cdot 10^{24}$. $\boldsymbol{R}_k$ is selected as large as possible so that the fuel consumption of the removal mission is minimized. To alleviate the effect on enlarging eccentricity, impulsive thrusts are applied per half orbit. The choice of optimal impulse epochs are not analyzed in this work.

The simulation results are presented in Fig. 13. From Fig. 13 we conclude that (1) the A/m is equal to 0.1 m^2/kg, and impulsive thrusts are applied to assist the removal process, (2) the final semimajor axis is about 28 km above the desired one, (3) the final perigee is just at the desired altitude, (4) the final eccentricity is within the desired range ([-0.003,0.003]), (5) the orbit inclination grows very large due to the third-body perturbation.

Although the final eccentricity is not perfectly reduced to zero, the final orbit still lies in the GEO graveyard region. Since the penalty matrix $\boldsymbol{R}_k$ is selected as large as possible, the fuel consumption of the removal mission is minimized, and a total impulse of 10.5 m/s is required.

5.3. Removing GEO satellites using only impulsive thrusts

To access the performance of the hybrid removal method, a comparative simulation is conducted. In this simulation, only impulsive thrusts are applied to the removal process. The system is linearized along the same nominal trajectory as in Section 5.2, and the penalty matrices are set as $\boldsymbol{S} = \mathrm{diag}\left[25, 10^{10}, 1\right] \cdot 10^{10}, \boldsymbol{Q} = \mathrm{diag}\left[25, 10^{10}, 1\right] \cdot 10^{5}, \boldsymbol{R} = \boldsymbol{I}_2 \cdot 10^{20}, \boldsymbol{Q}_{\mathrm{k}} = \boldsymbol{I}_3, \boldsymbol{R}_{\mathrm{k}} = \boldsymbol{I}_3 \cdot 10^{22}$. $\boldsymbol{R}_k$ is set to be smaller than in Section 5.2 so that more propellant can be applied in the removal mission. The impulsive thrusts are also applied per half orbit as in Section 5.2.

Simulation results are presented in Fig. 14, from which we can see that (1) the final semimajor axis is about 18 km above the desired one, (2) the final perigee is just at the desired altitude, (3) the final eccentricity is within the desired range ([−0.003, 0.003]). The magnitude of the acceleration due to SRP is equal to zero all the time and only impulsive thrusts are applied during the removal process. Debris is successfully removed to the GEO graveyard region with the use of a total impulse of 18.1 m/s. To compensate for the absence of SRP, 72.4% more amount of propellant is consumed than the hybrid method in Section 5.2.

6. Conclusions and future work

This work proposes an analytical solution for removal of end-of-life GEO satellites to the GEO graveyard region using SRP and impulsive thrusts. The main theoretical contribution of this work is the proposed hybrid disturbance-accommodation tracking maneuver. Simulation results indicate that, to remove a GEO satellite using only SRP, a minimal A/M ratio of 0.13 m^2/kg is required. When the A/M ratio of satellite is smaller than the minimal value, impulsive thrusts are applied to aid the removal process. For a satellite with A/M ratio of 0.1 m^2/kg, a total impulse of 10.5 m/s is required. The controller proposed in this work is also capable of placing the final inclination of the disposal orbit by judiciously choosing the penalty matrices.

Future work includes analyzing the optimal impulse epochs and finding the shortest removal time of both using only SRP and the hybrid approach.

References

Allen, J., 2010. The galaxy 15 anomaly: Another satellite in the wrong place at a critical time. Space Weather 8.

Anderson, P.V., Schaub, H., 2014. Local debris congestion in the geosynchronous environment with population augmentation. Acta Astronaut. 94, 619–628.

Anselmo, L., Pardini, C., 2008. Space debris mitigation in geosynchronous orbit. Adv. Space Res. 41, 1091–1099.

Athans, M., Falb, P.L., 2013. Optimal Control: An Introduction to the Theory and its Applications. Courier Corporation.

Bombardelli, C., Pelaez, J., 2011. Ion beam shepherd for contactless space debris removal. J. Guid. Control Dyn. 34, 916–920.

Borja, J.A., Tun, D., 2006. Deorbit process using solar radiation force. J. Spacecraft Rock. 43, 685–687.

Bryson, A.E., 2018. Applied Optimal Control: Optimization, Estimation and Control. Routledge.

Chao, C., 1998. Geosynchronous disposal orbit stability. In: AIAA/AAS Astrodynamics Specialist Conference and Exhibit, p. 4186.

Chun, H.M., Turner, J.D., Juang, J.N., 1985. Disturbance-accommodating tracking maneuvers of flexible spacecraft. J. Astronaut. Sci. 33, 197–216.

ESA, 2003. Executive summary of robotic geostationary orbit restorer, issue 1.0 (final issue), september 2003, esa. http://gsp.esa.int/documents/10192/43064675/C15678ExS.pdf/d4c58fae-33ab-4820-bc47-a66ca843093b.

ESA, 2018. Classification of geosynchronous objects. issue 20, revision 0. May 2018. esa. http://www.astronomer.ru/data/0128/Classification_of_Geosynchronous_Objects_I20R0.pdf.

Frey, S., Lemmens, S., Virgili, B.B., Flohrer, T., Gass, V., 2017. Impact of end-of-life manoeuvres on the collision risk in protected regions. Acta Astronaut. 138, 417–422.

Gopinath, N., Ganeshan, A., 2005. Long term evolution of objects in gso-disposal orbit. In: 4th European Conference on Space Debris, p. 291.

IADC, 2007. Inter-agency space debris coordination committee. space debris mitigation guidelines, revision 1, september 2007, iadc. http://www.unoosa.org/documents/pdf/spacelaw/sd/IADC-2002-01-IADC-Space_Debris-Guidelines-Revision1.pdf.

IERS, 2019. Earth orientation data, international earth rotation and reference systems service (iers). https://www.iers.org/IERS/EN/DataProducts/EarthOrientationData/eop.html.

Johnson, N.L., 2012. A new look at the geo and near-geo regimes: Operations, disposals, and debris. Acta Astronaut. 80, 82–88.

Kassebom, M., 2003. Roger-an advanced solution for a geostationary service satellite. In: 54th International Astronautical Congress of the International Astronautical Federation, the International Academy of Astronautics, and the International Institute of Space Law, pp. U–1..

Kelly, P.W., Bevilacqua, R., Mazal, L., Erwin, R.S., 2018. Tugsat: Removing space debris from geostationary orbits using solar sails. J. Spacecraft Rock. 55, 437–450.

Kitamura, S., Hayakawa, Y., Kawamoto, S., 2014. A reorbiter for large geo debris objects using ion beam irradiation. Acta Astronaut. 94, 725–735.

McInnes, C.R., 1999, . Solar Sailing Technology, Dynamics and Mission Applications, 1 ed., vol. 119. Springer Science & Business Media.

McKnight, D.S., Di Pentino, F.R., 2013. New insights on the orbital debris collision hazard at geo. Acta Astronaut. 85, 73–82.

Merino, M., Ahedo, E., Bombardelli, C., Urrutxua, H., Peláez, J., 2013. Ion beam shepherd satellite for space debris removal. Prog. Propul. Phys. 4, 789–802.

Oltrogge, D., Alfano, S., Law, C., Cacioni, A., Kelso, T., 2018. A comprehensive assessment of collision likelihood in geosynchronous earth orbit. Acta Astronaut. 147, 316–345.

Pelton, J.N., Jakhu, R., 2010. Space Safety Regulations and Standards. Elsevier.

Phipps, C.R., Bonnal, C., 2016. A spaceborne, pulsed uv laser system for re-entering or nudging leo debris, and re-orbiting geo debris. Acta Astronaut. 118, 224–236.

Rosengren, A.J., Alessi, E.M., Rossi, A., Valsecchi, G.B., 2015. Chaos in navigation satellite orbits caused by the perturbed motion of the moon. Mon. Not. R. Astron. Soc. 449, 3522–3526.

Schaub, H., Moorer, D.F., 2012. Geosynchronous large debris reorbiter: Challenges and prospects. J. Astronaut. Sci. 59, 161–176.

Sobiesiak, L.A., Damaren, C.J., 2014. Optimal continuous/impulsive control for lorentz-augmented spacecraft formations. J. Guid. Control Dyn. 38, 151–157.

Vallado, D.A., 2013. Fundamentals of astrodynamics and applications. vol. 12. fourth ed., Springer Science & Business Media.

Vatankhahghadim, B., Damaren, C.J., 2016a. Optimal combination of magnetic attitude control with impulsive thrusting. J. Guid. Control Dyn., 2391–2398

Vatankhahghadim, B., Damaren, C.J., 2016b. Optimal hybrid magnetic attitude control: Disturbance accommodation and impulse timing. IEEE Trans. Control Syst. Technol. 25, 1512–1520.

Vatankhahghadim, B., Damaren, C.J., 2017a. A cartesian relative motion approach to optimal formation flight using lorentz forces and impulsive thrusting. Acta Astronaut. 140, 255–263.

Vatankhahghadim, B., Damaren, C.J., 2017b. Magnetic attitude control with impulsive thrusting using the hybrid passivity theorem. J. Guid. Control Dyn. 40, 1860–1876.